

Supplementary Information: Pulse dynamics of flexural waves in transformed plates

Kun Tang¹, Chenni Xu^{1,2}, Sébastien Guenneau³, & Patrick Sebbah¹

¹ Department of Physics, The Jack and Pearl Resnick Institute for Advanced Technology, Bar-Ilan University, Ramat-Gan 5290002, Israel

² Zhejiang Province Key Laboratory of Quantum Technology and Device,

Department of Physics, Zhejiang University, Hangzhou, 310027, Zhejiang, China and

³ UMI 2004 Abraham de Moivre-CNRS, Imperial College London, London SW7 2AZ, United Kingdom

PERFORMANCES OF THE DESIGNED WAVESHIFTER WITH DIFFERENT BENDING ANGLES θ

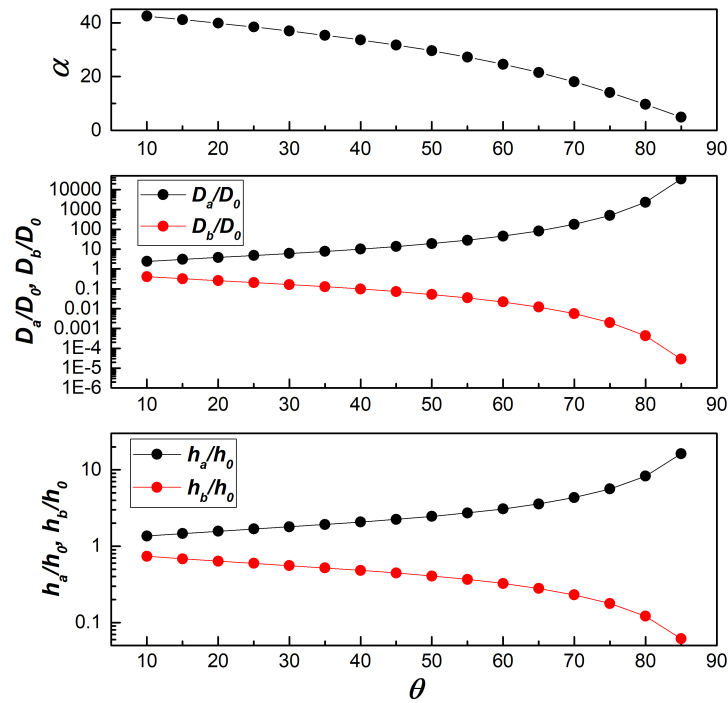


FIG. S1: Geometric parameters of the waveshifter dependence on bending angle θ . Plot of α , D_a (D_b), h_a (h_b) vs. θ , using Equation. (5) of the main article.

In the experimental investigation and numerical analysis presented in the main text, the bending angle θ of the waveshifter was chosen to be 20° . Here, we check the validity of our approach for larger values of θ . The dependence on θ of the plate rigidities D_a , D_b , the rotating angle α and the plates thicknesses h_a , h_b , are calculated following Equation. (5) and shown in Figure. S1, see also Figure. 1(b). When θ varies between 0 and 90° , α decreases gradually, while D_a and h_a diverge rapidly near 90° (notice the logarithmic scale in Figure. S1). This indicates that much stronger anisotropy is required for sharper bending angle θ .

Following the method presented in the main text, we design a waveguide with the same geometry as the waveshifter shown in Figure. 1, but with different bending angles θ , ranging from 30° to 70° . The corresponding values of α , h_a and h_b are directly obtained from Equation. (5). The out-of-plane velocity field distribution is calculated at 16kHz and shown in Figure. S2 with a comparison to the uniform bent waveguide without corrugation. For values of θ between 30° and 60° , the 0^{th} -order mode of the waveguide is efficiently transmitted beyond the bend, with the direction of its wavefront well preserved. In contrast, the same incident mode is seen to convert into a combination of even and odd higher-order modes in the uniform waveguide without corrugation. Beyond these values ($\theta \geq 70^\circ$), the waveshifter loses its characteristics: the wavefront direction is no longer preserved leading to mode conversion and

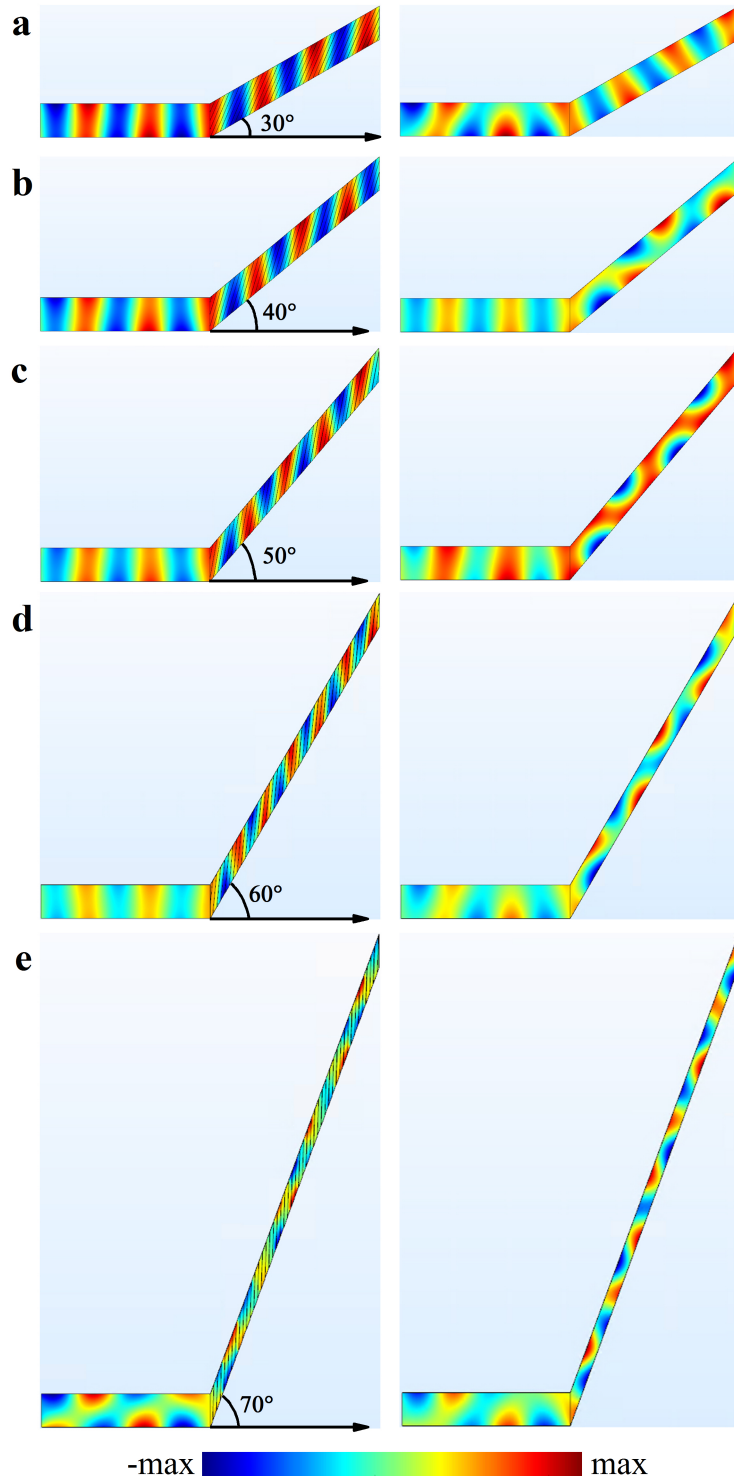


FIG. S2: Waveshifter with different bending angles θ . Left column: Simulated out-of-plane velocity field at $f = 16$ kHz for the waveshifter with different bending angles (a) $\theta = 30^\circ$, (b) $\theta = 40^\circ$, (c) $\theta = 50^\circ$, (d) $\theta = 60^\circ$ and (e) $\theta = 70^\circ$. Right column: Numerical simulations for the corresponding empty waveguides without any corrugation.

back-reflection. At these angles, the homogenization formula breaks down, which assumes a low, or at least moderate, contrast in material parameters.

We present in Figure. S3 snapshots of the velocity field distribution at three different times in response to a short

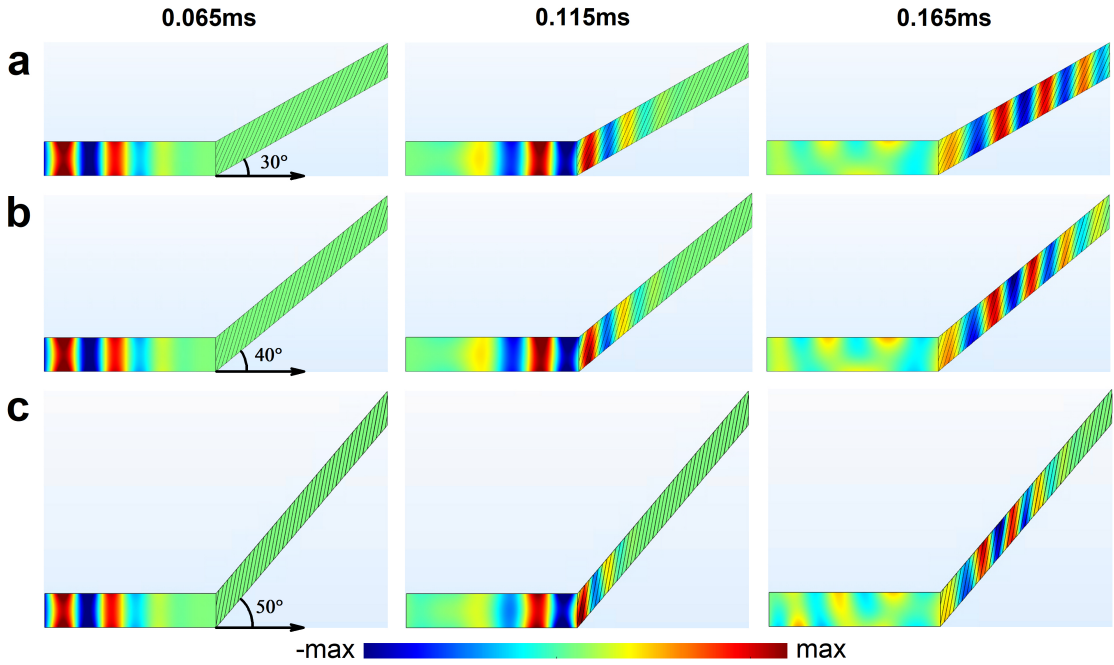


FIG. S3: Dynamics of pulse propagation in the waveshifter with different bending angles θ . (a) Full-3D numerical simulations: Snapshots of the out-of-plane velocity field calculated in response to a Ricker pulse with central frequency 20 kHz, at times 0.065 ms (left panel), 0.115 ms (middle panel), and 0.165 ms (right panel), for waveshifters with bending angles (a) $\theta = 30^\circ$, (b) $\theta = 40^\circ$, and (c) $\theta = 50^\circ$.

incident pulse, for bending angles ranging from 30° to 50° . The pulse is seen to propagate smoothly across the waveguide bend with negligible back-reflections, while the wavefront remains vertical, in the same direction as the incident wave. This confirms the performance for short pulses of our designed waveshifters for large bending angles, up to 50° . For larger angles θ and larger contrast in material parameters, local resonances occur in the long wavelength limit and the resulting effective parameters become dispersive. The metamaterial waveguide no longer approximates a dispersionless (frequency independent) transformed medium, and this has a deleterious impact on the metamaterial efficiency. In fact, the larger the contrast in material parameters, the more dispersion in effective parameters, and thus the more impact on the pulse propagation. The choice of $\theta = 20^\circ$ in the experimental demonstration presented in the main text is a good compromise between experimental constraints and large values of θ , the main restriction being the resolution of the 3D printing machine and the thickness h_b , which decreases rapidly with θ (see Figure. S1).

BROADBAND PERFORMANCE OF THE DESIGNED WAVESHIFTERS

In order to estimate the working bandwidth for designed waveshifters, we calculate the contribution of mode 0 to the total field for the waveshifter with bending angle of $\theta = 20^\circ$, in transmission $X > 0$. To do that, we define $|\eta_0| = \int dX |\eta(X)|$, $|\eta| = \int dX \int_0^H dY |\eta(X, Y)|$, where H is the width of the waveguide, $|\eta(X, Y)|$ is interpolated on a grid (X, Y) using the transformation $X = x$ and $Y = y - x \tan \theta$. The integrals are performed for $X > 0$ and we denote $|\eta_0| / |\eta|$ the weight of mode 0 in the transmission. As shown in Figure .S4, we compare the contribution of mode 0 in transmission for waveshifter with corresponding empty bent waveguide, under Perfectly Matched Layer (PML) boundary condition at the entrance and exit of the waveguide. The mode 0 remains largely dominant (above 90%) for all frequencies ranging from 0.1kHz to 30kHz (i.e. with a fractional bandwidth of 200%, black solid curve), while it decreases linearly for the corresponding empty bent waveguide (red solid curve).

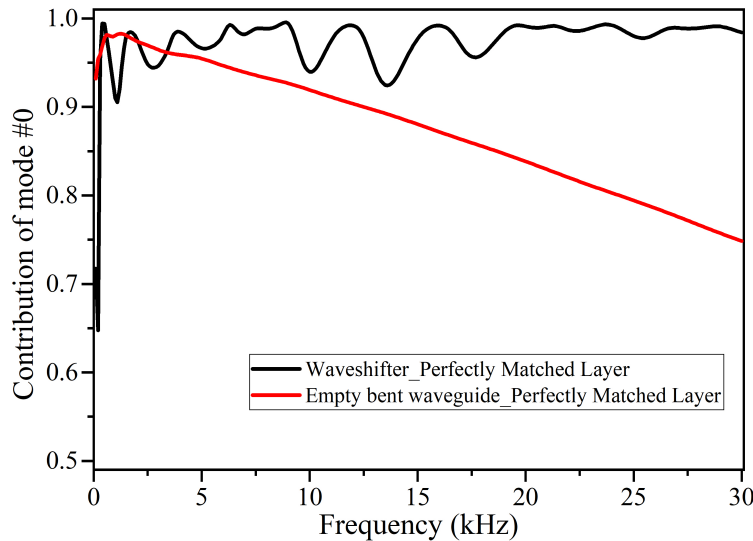


FIG. S4: Contribution of mode 0 to the total field in transmission $X > 0$ as a function of frequency for waveshifter (black color) and corresponding empty bent waveguide (red color) with bending angle of $\theta = 20^\circ$, supplied with Perfectly Matched Layer in the simulations.

CLOAKING

The waveshifter is an interesting device which can be used as the building block of a variety of new functional components, including wave splitters, combiners and invisibility cloak [1]. This is illustrated here with a cloaking device based on four waveshifters, arranged in a symmetric way around a diamond-shaped hole (see Figure. S5). Such a cloaking device has been proposed in [2] for continuous light waves and is demonstrated here for pulsed elastic waves. We use the parameters calculated earlier, θ , h_a , h_b , h_0 , and α , but instead of limiting the transformed region to a waveguide geometry, we simulate an incident pulse (Ricker pulse centered at 20 kHz) with a 160 mm-wide Gaussian wavefront propagating in a wide corrugated area around the diamond-shaped hole. Figure S5 compares the field distribution of the vertical elastic velocity resulting from the scattering by a bare hole with stress-free boundaries without and with the cloaking device, at three different time steps. The Gaussian wavefront splits as it hits the hole and the wavefront rapidly breaks apart. With the cloak however, the wavefront is maintained while following the edges of the obstacle and recombines after the hole. Beyond the hole, the initial Gaussian profile is restored. In addition to the invisibility effect, the cloak itself is invisible, with negligible back reflection. We checked that the temporal elongation of the pulse is solely due to flexural waves dispersion, as it would occur naturally in a plain plate without the obstacle.

Following this design, we construct a cloaking device for different values of θ . We use the parameters calculated in Figure. S2, h_a , h_b , h_0 , and α , for different values of θ . A Ricker pulse centered at 20 kHz with a 160 mm-wide Gaussian transverse profile is propagated in the direction of the hole. The field distribution of the out-of-plane velocity computed at time step 0.38ms, is shown in Figure. S6 for $\theta = 20^\circ$, $\theta = 30^\circ$, $\theta = 40^\circ$ and $\theta = 50^\circ$, for the diamond-hole with and without the cloaking corrugation. We find that the outgoing wave points in the same direction as the incident wave and that the incident wavefront is well restored for metamaterial cloaks with bending angles up to $\theta = 40^\circ$. This is in stark contrast with the field distributions resulting from the scattering by a bare hole (2nd row in Figure. S6), where the incident plane wavefront is seen to scatter off into multiple directions, and any information on the initial wavefront is lost. The cloaking device is therefore clearly effective to cloak even large diamond-shape holes, at least for diamond angles up to $\theta = 40^\circ$. For $\theta \geq 50^\circ$, the metamaterial cloak still refocuses efficiently the wavefront in the incident direction, but starts to yield significant wavefront distortions.

To better quantify the cloaking efficiency, we perform a spatial Fourier transformation to obtain the velocity amplitude in wave-vector (k) space (3rd and 4th row in Figure. S6). The simulated wave field in k space for metamaterial cloak is mainly localized around two sparkling lines, similar to wave propagation inside the plain plate, which indicates most of the energy points at the forward direction. However, the scattered wave by the bare hole is composed of a wider range of wave vectors located within an annulus regime. It means that the scattered wave no longer remains a forward plane wavefront and orient in multiple directions. This confirms that the metamaterial cloak refocuses

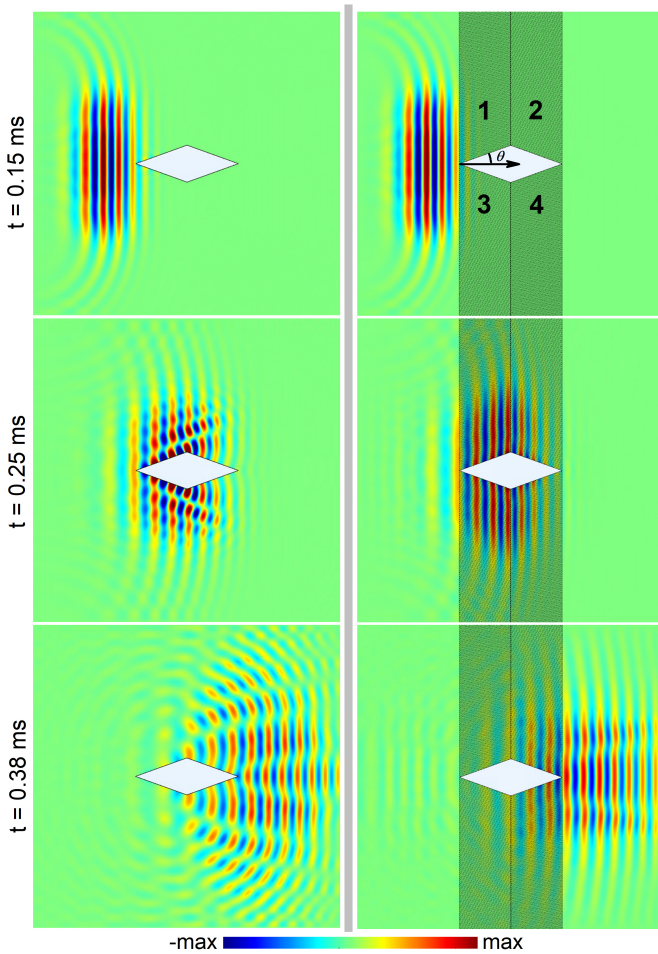


FIG. S5: Cloaking flexural waves with 4 waveshifters. Full-3D elastic-wave transient simulations of elastic field distribution resulting from the propagation of a pulsed gaussian wave (Ricker pulse centered at 20 kHz) with 160 mm-wide transverse profile, at times $t=0.15$ ms, $t=0.25$ ms, $t=0.38$ ms. (left panel) Bare diamond-shaped hole; (right panel) diamond cloak. The cloak is composed of 4 corrugated regions around a diamond-shaped hole with $\theta=20^\circ$, as defined in the figure. Geometric parameters of the corrugated region 1 are identical to those of the waveshifter of Figure. 1. Region 3 is the mirror image of Region 1 with respect with the horizontal axis. Regions 2 and 4 are mirror images of Region 1 and 3 with respect to the vertical axis. One notes that scattering off the hole is nearly suppressed by the corrugated regions at time step $t = 0.38\text{ms}$: The cloak flattens the concentric wavefronts emanating from the hole. See Figure. S4 in [Supplementary Information] for same simulations performed for holes and cloaked holes with larger θ .

efficiently the wavefront in the incident direction for bending angles up to $\theta = 50^\circ$.

The waveshifter can thus be viewed as a building block for certain types of diamond shaped cloaks, such as shown in Fig. S6. Nonetheless, in the similar way to the waveshifter, a diamond cloak design is constrained by the requirement of a moderate contrast in material parameters that approximate the transformed plate medium, which is dictated by the angle θ inside the diamond shaped hole. The increasing dispersion of the effective medium induced by the increasing contrast in material parameters (here the layers' thicknesses), leads to an increased distortion of the Ricker pulse for large θ , as becomes clear for $\theta = 50^\circ$. In fact, the physical phenomenon of effective dispersion induced by large contrast in materials parameters of periodic structures occurs for any type of waves, so similar constraints exist for acoustic and electromagnetic cloaks: The price to pay for a cloak suppressing the scattering of a large object is the requirement of a large anisotropy of the transformed medium, which will then be approximated by periodic structures with large contrast in material parameters. Therefore such cloaks might work well in theory throughout a large frequency band when using homogenization approaches to mimic the transformed media, but their efficiency will in practice remain moderately low for Ricker pulses due to the inherent dispersion in the effective parameters.

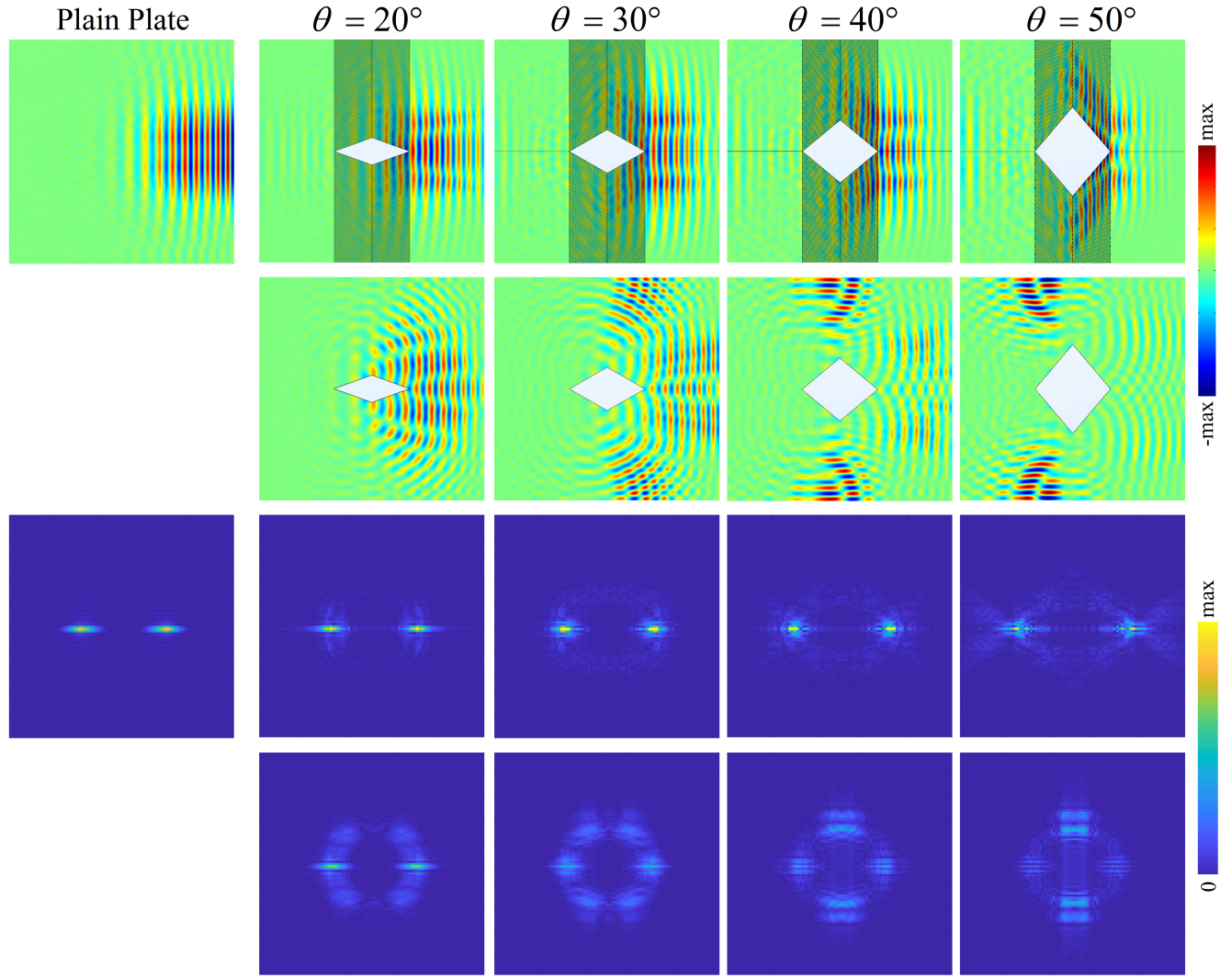


FIG. S6: Diamond-shape cloak with increasing angle θ . Full-3D elastic-wave transient simulations of elastic field distribution at time step 0.38 ms: (1st column) for the plain plate; (1st row) for the diamond cloak composed of four corrugated regions, (2nd row) for the bare diamond-shaped hole, with bending angles (2nd column) $\theta = 20^\circ$, (3rd column) $\theta = 30^\circ$, (4th column) $\theta = 40^\circ$, (5th column) $\theta = 50^\circ$. Spatial Fourier transformation is performed on the velocity field shown in the 1st and 2nd rows to obtain the velocity amplitude in wave-vector space shown in 3rd and 4th rows.

EIGENMODES OF THE WAVEGUIDE

Here we provide a short explanation on calculating the flexural eigenmodes supported by homogeneous plate with stress-free boundaries. The details can be found in ref. [3]. As Kirchhoff-Love plate equation is of fourth order, there exist two sets of modes at each frequency

$$w^{(e)}(y) = A \left[\cosh\left(\frac{\chi_m W}{2}\right) \cosh(\chi_p y) - \frac{k^2 \nu - \chi_p^2}{k^2 \nu - \chi_m^2} \cosh\left(\frac{\chi_p W}{2}\right) \cosh(\chi_m y) \right] \quad (1)$$

$$w^{(o)}(y) = A \left[\sinh\left(\frac{\chi_m W}{2}\right) \sinh(\chi_p y) - \frac{k^2 \nu - \chi_p^2}{k^2 \nu - \chi_m^2} \sinh\left(\frac{\chi_p W}{2}\right) \sinh(\chi_m y) \right] \quad (2)$$

Where $\chi_p = \sqrt{k^2 + K^2}$, $\chi_m = \sqrt{k^2 - K^2}$, $K^2 = \omega\sqrt{\rho h/D}$, and A is a normalization constant such that $\int_{-W/2}^{W/2} dy |w^{(o,e)}(y)|^2 = 1$. The dispersion relations $\omega(k)$ can be derived by solving the following transcendental equations

$$[K^2 + (1 - \nu)k^2]^2 \chi_m \tanh(\chi_m W/2) = [K^2 - (1 - \nu)k^2]^2 \chi_p \tanh(\chi_p W/2) \quad (3)$$

for even modes, and

$$[K^2 + (1 - \nu)k^2]^2 \chi_m \coth(\chi_m W/2) = [K^2 - (1 - \nu)k^2]^2 \chi_p \coth(\chi_p W/2) \quad (4)$$

for odd modes.

It yields the wavenumber $k_i^{(o,e)}$ associated to each mode $w^{(o,e)}$ at frequency ω . The y -dependence of the first two even and odd eigenmodes is shown in Fig. 3(a). The mode profile of first even mode (mode 0) is close to a plane wavefront.

ANIMATIONS OF THE PULSES PROPAGATION INSIDE WAVESHIFTER AND ROTATOR.

The pulse dynamic propagation of the measured and simulated wave patterns inside waveshifter and rotator are shown in the enclosed videos.

- Video: “waveshifter-experiment”, “waveshifter-simulation”.

Measured and simulated time evolution of the spatial distribution of the displacement for wave propagation through designed waveshifter. The incident pulse is a Ricker pulse with peak frequency $f_0 = 20kHz$.

- Video: “rotator-experiment”, “rotator-simulation”.

Measured and simulated time evolution of the spatial distribution of the displacement for wave propagation through designed rotator. The incident pulse is a Ricker pulse with peak frequency $f_0 = 4kHz$.

- Video: “mirage effect-vertical scatter”, “mirage effect-rotated scatter”, “mirage effect-rotated scatter with outside rotator”.

Simulated time evolution of the spatial distribution of the displacement through bare vertical scatter, rotated scatter, and rotated scatter with outside rotator. The incident pulse is a Ricker pulse with peak frequency $f_0 = 4kHz$.

- Video: “1D cloak-void”, “1D cloak-void with a cloak”.

Simulated time evolution of the spatial distribution of the displacement for wave propagation through a bare diamond-shaped void or void coated with a one-dimensional cloak. The incident pulse is a Ricker pulse with peak frequency $f_0 = 20kHz$.

-
- [1] M. Rahm, S. A. Cummer, D. Schurig, J. B. Pendry, D. R. Smith, *Phys. Rev. Lett.* **2008**, 100 063903.
[2] H. Chen, C. T. Chan, *Phys. Rev. B* **2008**, 78 054204.
[3] M. C. Cross, R. Lifshitz, *Phys. Rev. B* **2001**, 64 085324.